


2015

# 2D measurements of turbulence & mixing driven by internal waves impinging on a slope

Zhimin Li

*Iowa State University*

Follow this and additional works at: <https://lib.dr.iastate.edu/etd>

 Part of the [Civil Engineering Commons](#), and the [Environmental Engineering Commons](#)

---

## Recommended Citation

Li, Zhimin, "2D measurements of turbulence & mixing driven by internal waves impinging on a slope" (2015). *Graduate Theses and Dissertations*. 14372.

<https://lib.dr.iastate.edu/etd/14372>

This Thesis is brought to you for free and open access by the Iowa State University Capstones, Theses and Dissertations at Iowa State University Digital Repository. It has been accepted for inclusion in Graduate Theses and Dissertations by an authorized administrator of Iowa State University Digital Repository. For more information, please contact [digirep@iastate.edu](mailto:digirep@iastate.edu).

**2D measurements of turbulence & mixing driven by internal waves impinging on a slope**

by

**Zhimin Li**

A thesis submitted to the graduate faculty  
in partial fulfillment of the requirements for the degree of

MASTER OF SCIENCE

Major: Civil Engineering

Program of Study Committee:  
Chris Rehmann, Major Professor  
Hui Hu  
Roy Gu

Iowa State University

Ames, Iowa

2015

## TABLE OF CONTENTS

LIST OF FIGURES .....	iii
LIST OF TABLES .....	v
ABSTRACT.....	vi
CHAPTER 1. INTRODUCTION .....	1
CHAPTER 2. EXPERIMENTS AND METHODS .....	5
Measurements .....	5
Experimental Facility .....	7
Processing .....	10
Summary of Experimental Procedure .....	12
CHAPTER 3. RESULTS AND DISCUSSION .....	14
Properties of the Incident Wave.....	14
Velocity Fields .....	18
Dissipation Fields.....	20
Implications for mixing.....	28
CHAPTER 4. CONCLUSIONS .....	31
APPENDIX A. WAVEMAKER NOTES .....	33
APPENDIX B. MSCTI PROBE & CALIBRATION .....	35
REFERENCES .....	40
ACKNOWLEDGMENTS .....	41

## LIST OF FIGURES

Fig. 1. Dimensional analysis parameters. ....	3
Fig. 2. Experimental facility. ....	5
Fig. 3. Wavemaker configuration & components. ....	6
Fig. 4. Schematic of the particle image velocimetry system. ....	8
Fig. 5. System for ensuring PIV measurements occur at specified phases. ....	10
Fig. 6. PIV raw image with mask and boundary. ....	11
Fig. 7. Salinity signals measured by the MSCTI at a fixed point. ....	15
Fig. 8. Wavelength determination from velocity fields of PIV. ....	16
Fig. 9. Negative correlation between $\zeta_0/A$ and $\omega/N$ . ....	17
Fig. 10. Velocity fields from PIV. ....	19
Fig. 11. 2D dissipation distribution in Case 2. ....	21
Fig. 12. PIV image with reflection. ....	22
Fig. 13. Dissipation fields on a 15° slope. ....	22
Fig. 14. Dissipation fields on a 30° slope. ....	23
Fig. 15. Comparison of dissipation fields with different slope. ....	24
Fig. 16. Comparison of dissipation fields with different $\omega$ and $N$ . ....	24
Fig. 17. Profile of dissipation in Case 2. ....	25
Fig. 18. $h_{\text{meas}}/h_{\text{pred}}$ as a function of $\gamma$ . ....	26
Fig. 19. The comparison of dissipation with TKE. ....	27
Fig. 20. Spatially-averaged dissipation as a function of phase. ....	28
Fig. B.1. MSCTI configuration. ....	37
Fig. B.2. MSCTI calibration for $V_{\text{toff}}$ and $V_{\text{coff}}$ . ....	37

Fig. B.3. Curve of response equation B.1 .....39

Fig. B.4. Curve of response equation B.5 .....39

**LIST OF TABLES**

Table 1. Summary of experimental parameters. ....	13
Table 2. Wavelengths and boundary layer thicknesses. ....	14
Table 3. Wave amplitudes. ....	17
Table B.1. MSCTI specifications .....	36

## ABSTRACT

Fluxes in stratified water bodies such as lakes and oceans are often controlled by turbulence and mixing at sloping boundaries. One mechanism of boundary mixing is the reflection of internal waves from slopes; when the angle  $\alpha$  that the internal wave ray makes with the horizontal is equal to the slope angle  $\beta$ —that is, when the ratio  $\gamma = \sin\alpha/\sin\beta = 1$ , critical reflection occurs. Critical reflection is thought to increase vertical mixing in lakes and contribute to the shaping of continental shelves in the ocean. Experiments were conducted to measure in detail the turbulence generated by near-critical and supercritical internal waves impinging on a slope. Velocity fields were measured with particle image velocimetry (PIV) and used to derive two-dimensional fields of dissipation. Harmonics were observed in the velocity fields in some cases with  $\gamma \geq 1$ , and the angle of the harmonics agreed with theoretical predictions of others. The highest dissipation was patchily distributed near the slope, and it formed a layer whose thickness was within 20-25% of the values predicted by previous researchers. For supercritical waves ( $\gamma > 1$ ), high values of dissipation were not confined solely in a layer near the slope. The high dissipation also appeared in regions with reflecting waves, harmonics, and—in some cases—the incident waves. Regions of high turbulent kinetic energy coincided with regions of high dissipation for all cases. Values of  $\varepsilon/\nu N^2$  were small near the slope. Maximum values were  $O(1)$ , while values based on cycle-averaged dissipation were less than 0.2. In these cases, the patchy nature of the dissipation suggests that little mixing will occur.

## CHAPTER 1. INTRODUCTION

In stratified water bodies such as oceans and lakes, the transport of nutrients, sediment and microorganisms is usually controlled by turbulence and mixing at the sloping boundaries (Ivey, Winters, & De Silva, 2000). Wind sets up the water surface, and the isotherms tilt and generate internal waves. The internal waves propagate to and break on the sloping boundary, which can cause turbulence and mixing near the boundary especially when critical reflection happens. MacIntyre et al. (1999) found that the eddy diffusivity onshore at the depth where the thermocline intersected the shore was 4 orders of magnitude higher than the eddy diffusivity at the same depth offshore in Mono Lake. Internal waves critically reflecting on the continental slope off Northern California and New Jersey can lead to high bottom velocities and bottom shear stresses that can contribute to shaping the continental slopes (Cacchione et al., 2002). Hence, the study of quantifying the dynamics of turbulence and mixing on the benthic boundary layer has become an important aspect of oceanology and limnology.

The reflection of internal waves from a sloping boundary depends on the angle of the internal wave ray and the angle of the boundary. Internal waves excited by monochromatic oscillation in a stratified flow propagate at an angle

$$\alpha = \sin^{-1} \left( \frac{\omega}{N} \right), \quad (1)$$

to the horizontal, where  $\omega$  is the frequency of the monochromatic oscillation,  $N = [-(g / \rho_0) \partial \rho / \partial z]^{1/2}$  is the buoyancy frequency,  $g$  is the acceleration of gravity,  $\rho_0$  is the reference density, and  $\partial \rho / \partial z$  is the background density gradient. If  $\beta$  is the angle of the boundary with respect to the horizontal, then the reflection is determined by the parameter



$\gamma = \sin \alpha / \sin \beta$ . Low-frequency waves ( $\gamma < 1$ ) will be reflected back into the interior, while high-frequency waves ( $\gamma > 1$ ) will be reflected up the slope and eventually break. Critical reflection occurs when the angle of the wave ray equals the angle of the sloping boundary ( $\gamma = 1$ ). In this case, a large portion of incident wave energy is dissipated along the boundary, and turbulent mixing can occur (McPhee-Shaw & Kunze, 2002). However, Ivey et al. (1995) found that the turbulent mixing could occur when  $\gamma > 1$  and the turbulence is even more vigorous than the critical condition, especially when  $1.5 < \gamma < 2$ .

Dimensional analysis identifies parameters controlling the mixing caused by internal waves on a slope (Fig. 1). For example,  $\varepsilon$ , the rate of dissipation of turbulent kinetic energy (TKE), could depend on the geometry of the water body (length  $L$ , width  $B$ , and depth  $H$ ); properties of the slope such as the slope angle  $\beta$ ; properties of the fluid such as buoyancy frequency  $N$  and kinematic viscosity  $\nu$ ; properties of the waves such as the frequency  $\omega$ , wavelength  $\lambda$ , amplitude  $\zeta_0$  of isopycnal displacement; and wavemaker amplitude  $A$ . Assuming that the waves are two-dimensional, that the isopycnal displacement can be related to the amplitude of the wavemaker, and that the length, width, and depth are large enough to be ignored, then one can write:

$$\varepsilon = f(\beta, \omega, N, \nu, A, \lambda) \quad (2)$$

After the slope angle is combined with the buoyancy frequency to get the critical frequency  $N \sin \beta$ , dimensional analysis gives

$$\frac{\varepsilon}{\nu N^2} = f\left(\gamma, \frac{A}{\lambda}, \frac{NA^2}{\nu}\right) \quad (3)$$

Most studies, including this one, focus on the effect of  $\gamma$  on the reflection and resulting flow

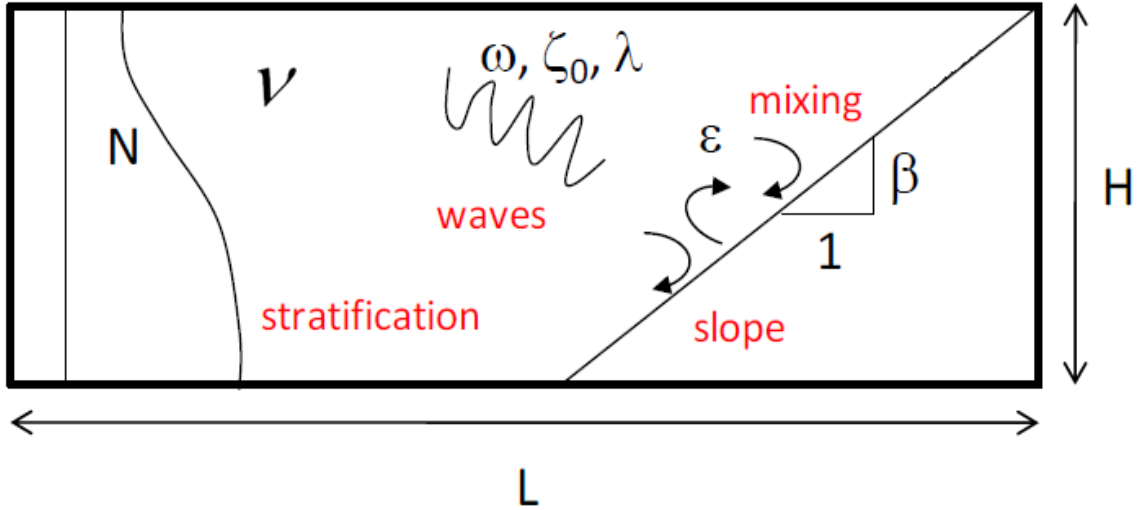


Fig. 1. Dimensional analysis parameters.

and mixing, but equation (3) shows that the wave steepness  $A/\lambda$  and the parameter  $NA^2/\nu$ , which is related to the Grashof number, a parameter that measures the relative importance of buoyancy and viscosity.

Dissipation from reflecting internal waves was measured by Ivey et al. (2000). They used the Portable Flux Probe to measure the one-dimensional dissipation distribution, and they derived an estimate of the cycle-averaged dissipation based on the boundary layer thickness. In the long-term turbulence measurements of Lorke (2007) in a lake, dissipation inside a boundary layer on the slope exceeded the dissipation outside by two orders of magnitude. Direct numerical simulations of Chalamalla et al. (2013) showed a correlation between TKE and dissipation. Rodenborn et al. (2011) used particle image velocimetry (PIV) to study the harmonics occurring when internal waves impinge on a slope.

The dissipation rate indicates the conversion of TKE into thermal internal energy and dissipation fields demonstrate the location where the high conversion rate—in other words, vigorous mixing—occurs. Hence, the goal of the present work is to measure 2-D fields of velocity and turbulence quantities, such as the dissipation of TKE with PIV and to explore

the relation of dissipation and TKE and other relevant parameters. Hence, a laboratory model was set up to imitate the internal wave impinging on a sloping boundary in oceans and lakes. The experimental facility and methods are described in Chapter 2, and results on internal wave properties, velocity fields, and turbulence properties are presented and discussed in Chapter 3. Chapter 4 summarizes the main conclusions and presents recommendations for future work.

## CHAPTER 2. EXPERIMENT AND METHODS

### A. Experimental Facility

The experiment was conducted in a rectangular Plexiglas tank of length 304.80 cm, width 40.64 cm, and total depth 55.88 cm (Fig. 2). The tank was reinforced with T-slotted aluminum framing beams (80/20® Inc.) to prevent deformation when filled with water and allow other equipment to be installed above the tank. A Plexiglas slope with an angle  $\beta$  of either  $15^\circ$  or  $30^\circ$  was used. Each slope had a connected plate so that they could be easily attached to the tank at the right angle. The slopes were 1.27 cm thick and 38.10 cm wide. The slope thickness cannot be too small as the slope material's self-weight causes deformation,

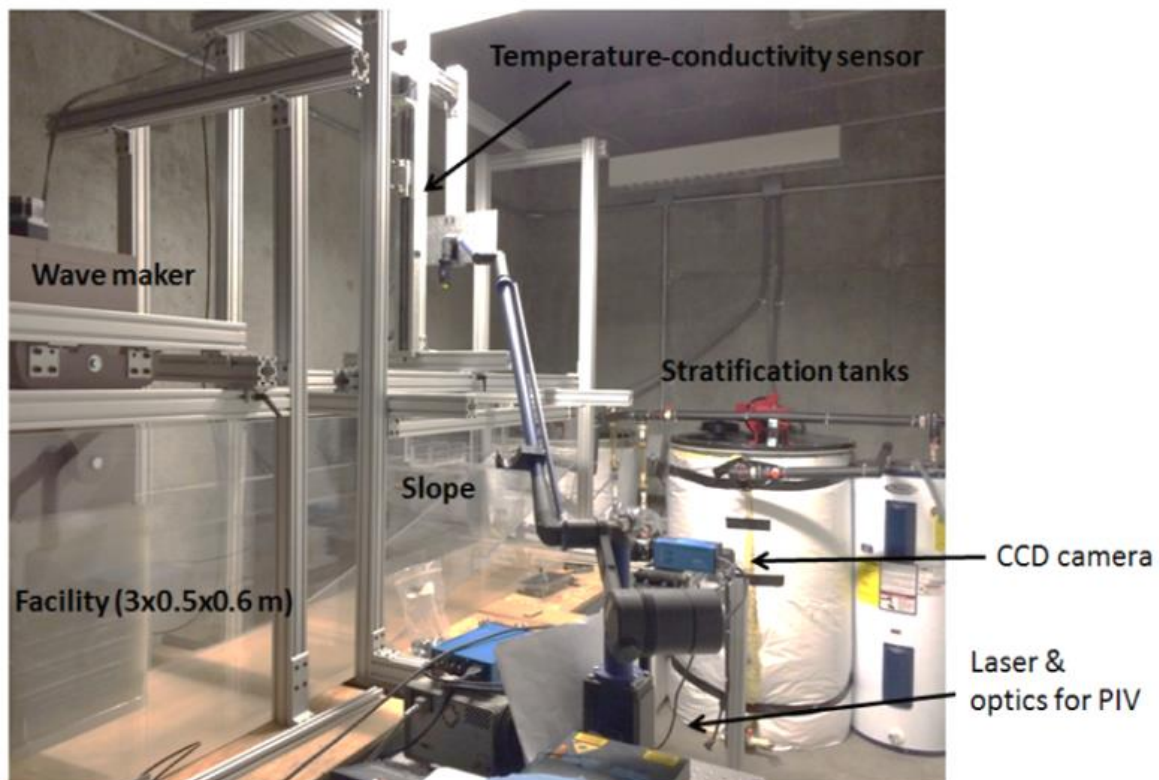


Fig. 2. Experimental facility. The stratification tanks and wavemaker as well as instruments for measuring temperature and salinity profiles and velocity fields are also shown.

and the width of slopes is 2.5 cm smaller than the inner width of facility tank to allow water to pass.

Waves were generated with a wavemaker that followed the design of Gostiaux et al. (2007), shown in Fig. 3. The wavemaker consists of a stack of 12 eccentric disks with diameter of 7.62 cm, which are strung together by a main shaft. The hole for the main shaft was drilled eccentrically in the disks to give them an amplitude of oscillation of 1 cm. Each disk has 11 holes surrounding the main hole for a secondary shaft to offset adjacent disks by  $32.73^\circ$ , and the disks were assembled as a helical stack so that the first and last wheels were at the same phase. The stack of disks is mounted in 12 plates with rectangular holes. The width of the holes matched the diameter of the disks, and the length of the holes was twice

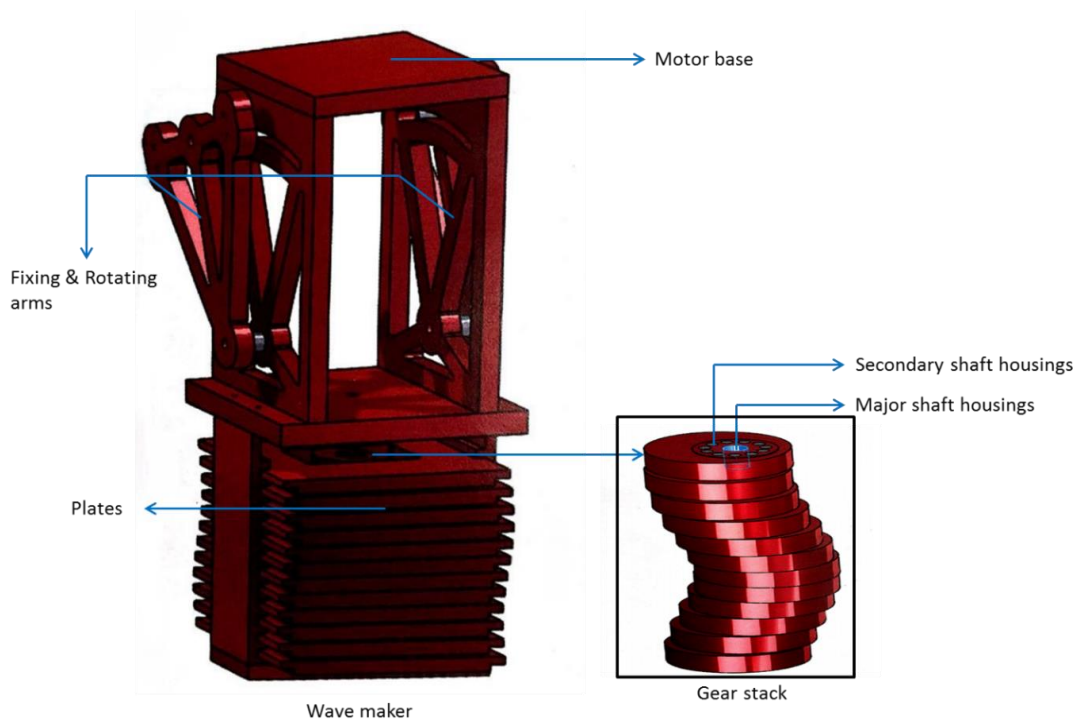


Fig 3. Wavemaker configuration & components (excluding shafts).

the diameter of the disks so that the disks can drive the plates in one direction. The plates are made by a type of waterproof foam board called RenShape which makes them buoyantly balance in the water and dramatically reduces the mechanical friction of the wavemaker. The assembled stack and plates were enclosed in a half-opened box. The plates were placed in slots in two sides of the box. To decrease friction, a space of 0.2 cm was maintained between the disk stack and plates and the plates and the box. The space cannot be too much or the plates will wobble in the box and fail to generate an ideal sine wave. The upper part of the wavemaker allowed it to be fixed to the tank, and the rotating arms allowed it to be tilted. The disks and plates were driven with a high-torque gear motor (with 40.32 kg-cm holding torque). See Appendix A for more details on the wavemaker.

The double bucket method was employed to set linear stratification (Fortuin 1960). The first tank held fresh water, and the second held salty water. Water was pumped from the first tank to the second and stirred with a propeller. The mixture was pumped to the experimental tank through a diffuser that minimized mixing during filling. As the water in the second tank becomes lighter and lighter, the stratification sets up from denser water at bottom to the lighter water at top in experimental tank. The flowrate from the second tank to the experimental facility was twice the flowrate from the first tank to the second so that a linear stratification could be established.

## **B. Measurements**

Salinity and temperature were derived from measurements with a Precision Measurements Engineering Model MicroScale Conductivity-Temperature Instrument (MSCTI) system (See more details in Appendix B). The MSCTI is composed of a combined

probe and an electronic bridge. The combined probe consists of a thermistor and a conductivity probe with gap of approximately 1 mm guaranteeing the measurements coincide at the same location in the water body. Because the combined probe provides analog voltage outputs, the LabVIEW platform was applied to translate the analog data into salinity and temperature. The electronic bridge box allows the gains on the conductivity and temperature sensors to be adjusted. The MSCTI was calibrated against solutions of known temperature and salinity. The profiling of temperature and salinity was automated by a motor driven electro-mechanical assembly UniSlide®, which was also controlled with the LabVIEW platform. Properties of the incident wave were measured by setting the MSCTI at a fixed point in the incoming wave beam, collecting time series of temperature and conductivity, and removing noise by applying a low-pass filter.

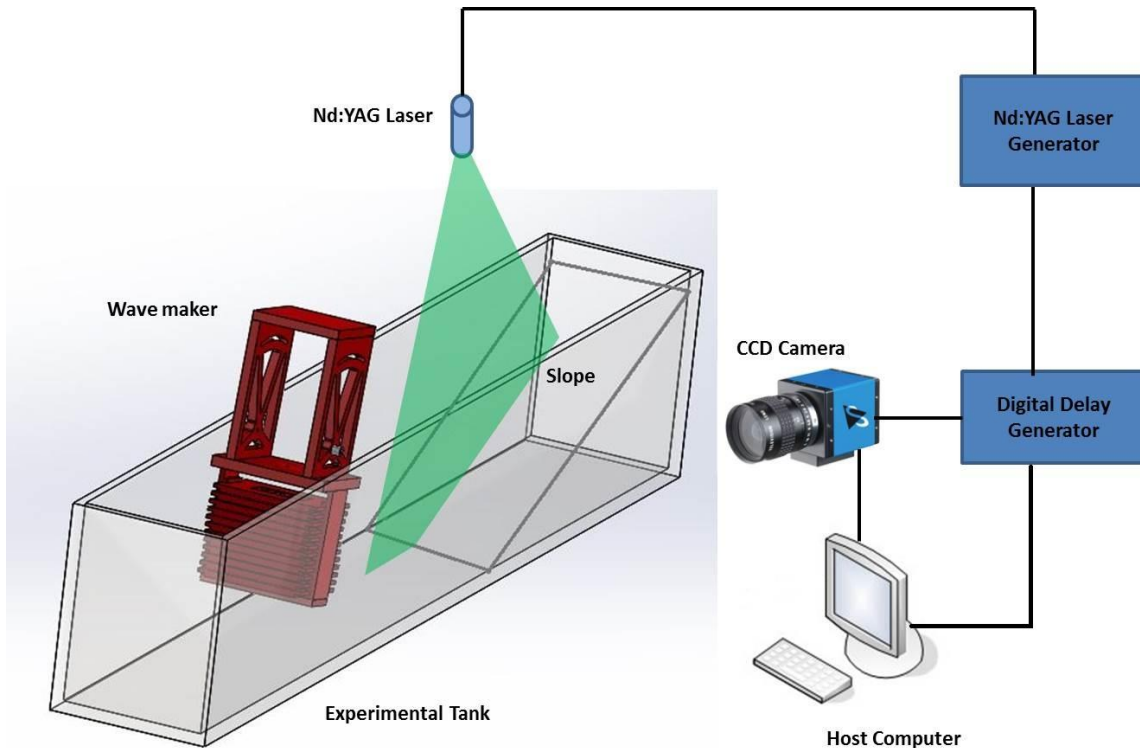


Fig. 4. Schematic of the particle image velocimetry system.

A high-resolution digital Particle Image Velocimetry (PIV) system was used to measure velocities (Fig. 4). The system was composed of a CCD camera, a digital delay generator and a laser generator. The flow was seeded with HGS silver-coated hollow spheres, and a laser sheet was created with an Nd:YAG laser (NewWave Gemini 200) emitting two pulses of 200 mJ at a wavelength of 532 nm. The laser beam was shaped to a sheet with thickness of 2 mm by a set of mirrors along with spherical and cylindrical lenses. Dark boards were used to cover the non-observable region to minimize the reflection from high energy illumination. Images were acquired with a 14-bit CCD camera (PCO2000, CookeCorp) with resolution of 2048 x 2048 pixels. The camera was aligned to face perpendicular to the laser sheet. A digital delay generator (Berkeley Nucleonics, Model 565) was used to control the time difference of illumination and image acquisition, and it connected both the CCD camera and the laser to a host computer (Hu, Yang, & Sarkar, 2011). To acquire images at specified phases of the wave, a tachometer was applied to trigger the illumination (Fig. 5). Each revolution of the wavemaker was divided into 12 phases, and once the wavemaker reached a new phase, the camera and laser were activated twice separated by  $\Delta t = 0.25$  s. This time interval was chosen to keep the pixel displacements less than  $\frac{1}{4}$  of the interrogation window size and to improve the correlation from frame to frame. Therefore, for an interrogation window with 32 x 32 pixels, the pixel displacement should be less than 8 pixels (Raffel et al. 2007). In our experiments the displacement was controlled at 4-5 pixels as the maximum particle speed varied from 2.5 mm/s to 3.5 mm/s.

The image resolution was set so that the dissipation of turbulent kinetic energy could be measured. Saarenrinne & Piirto (2000) recommended having the vector spacing  $\Delta x$  less than  $3\eta$ , where  $\eta = (\nu^3/\varepsilon)^{1/4}$  is the Kolmogorov scale and  $\nu$  is the kinematic viscosity. In the



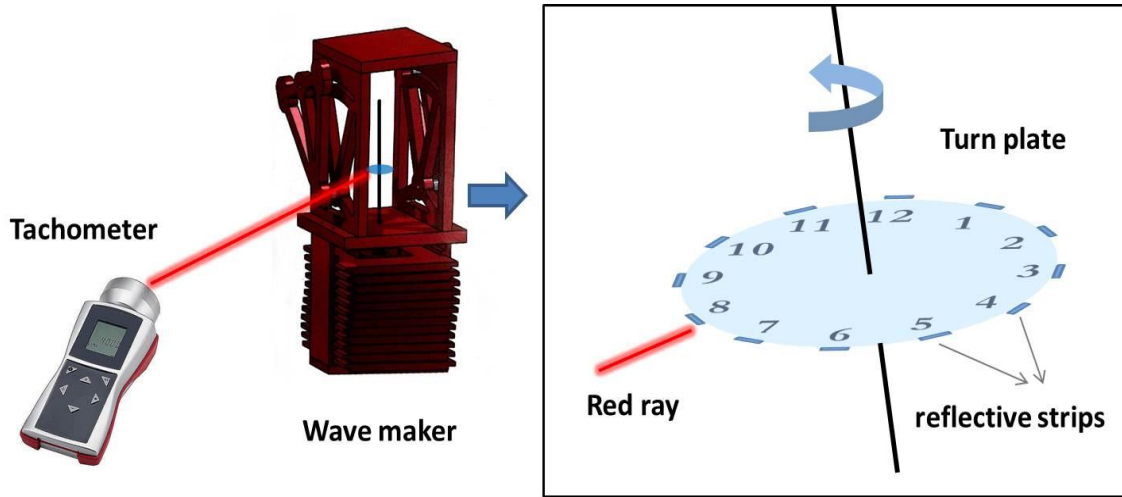


Fig. 5. System for ensuring PIV measurements occur at specified phases.

experiments, the image size of 327.5 x 327.5 mm for Case 1-4 and 336.7 x 336.7 mm for Case 5-9 combined with 2048 pixels in one direction and 32 pixels in one direction in the interrogation window yields  $\Delta x = 2.5$  mm. Because initial experiments indicated a maximum dissipation of the order  $10^{-6} \text{ m}^2/\text{s}^3$ , the corresponding Kolmogorov scale  $\eta$  was thus calculated as 1 mm. Therefore, the resolution of PIV image with  $\Delta x = 2.5$  mm met the criterion of vector spacing of Saarenrinne and Piirto (2000).

### C. Processing

Velocities were computed with PIV using a frame to frame cross-correlation technique. The interrogation window had 32×32 pixels, and the technique used an effective overlap of 50%. Also, the high exposure area near the slope was cut off to avoid miscorrelation (Fig. 6). Once the velocities were known, they were subjected to a triple decomposition. For example, the instantaneous velocity  $u$  is written as

$$u = \bar{u} + u + u' \quad (4)$$

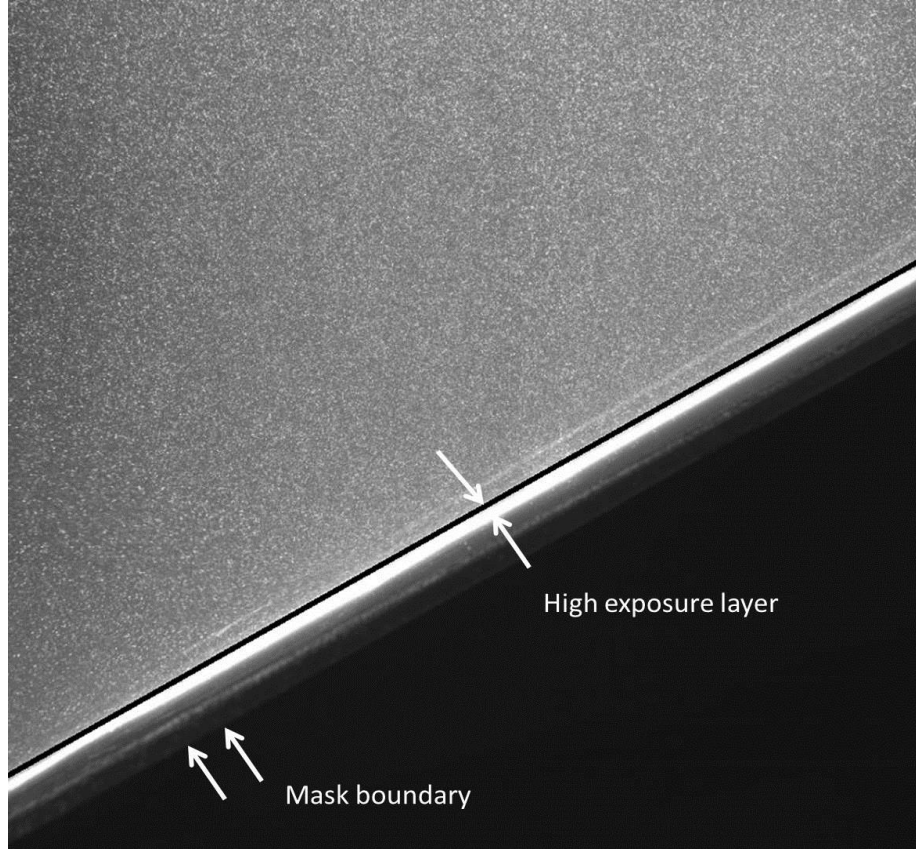


Fig. 6. PIV raw image. The figure shows mask boundary and high exposure layer. All zones below the black line were cut off during the processing.

where  $\bar{u}$  is the time-averaged velocity,  $u$  is the phase-averaged velocity, and  $u'$  is the fluctuating velocity.

Turbulence quantities were derived from the velocity fields. To account for unmeasured velocities and their derivatives, the turbulence was assumed to be axisymmetric about the vertical ( $z$  or  $x_3$  axis). Therefore, turbulent kinetic energy, defined as  $q^2 / 2 = \langle u_i'^2 \rangle / 2$ , was computed as  $q^2 / 2 = \langle u_1'^2 \rangle + \langle u_3'^2 \rangle / 2$ . The dissipation is defined as

$$\varepsilon = \nu \left\langle \frac{\partial u'_i}{\partial x_j} \left( \frac{\partial u'_i}{\partial x_j} + \frac{\partial u'_j}{\partial x_i} \right) \right\rangle = \nu (D_{ijj} + D_{iji}) \quad (5)$$

where

$$D_{ijpq} = \left\langle \frac{\partial u'_i}{\partial x_p} \frac{\partial u'_j}{\partial x_q} \right\rangle \quad (6)$$

so that

$$\begin{aligned} \varepsilon = \nu \left[ 2(D_{1111} + D_{2222} + D_{3333} + D_{1221} + D_{1331} + D_{2332}) \right. \\ \left. + D_{1122} + D_{2211} + D_{1133} + D_{3311} + D_{2233} + D_{3322} \right] \end{aligned} \quad (7)$$

The assumption of axisymmetry about the vertical axis leads to  $D_{2222} = D_{1111}$ ,  $D_{2233} = D_{1133}$ ,

$D_{3322} = D_{3311}$ , and  $D_{2332} = D_{1331}$ , and the results of George and Hussein (1991) lead to

$$D_{1122} = D_{2211} = 3D_{1111} - D_{3333} \quad (8)$$

$$D_{1221} = D_{2112} = \frac{1}{6}D_{3333} - \frac{1}{3}D_{1122} = \frac{1}{2}D_{3333} - D_{1111} \quad (9)$$

Substituting these results into equation (7) allows the dissipation to be expressed as

$$\frac{\varepsilon}{\nu} = 8D_{1111} + D_{3333} + 2D_{1133} + 2D_{3311} + 4D_{1331} \quad (10)$$

Gradients were computed with centered differences in the interior and forward differences on the edges.

#### D. Summary of Experimental Procedure

Experiments started with establishing the stratification. The PIV seeding material was mixed in both storage tanks used in the double-bucket method, and the facility was filled to a depth of 40 cm with a linear salt stratification. The initial density profile was measured, and the wave ray angle  $\alpha$  and wave frequency  $\omega$  were computed from the buoyancy frequency and desired value of  $\gamma$ . The wavemaker was tilted to the angle  $\alpha$ , and waves were generated for at least 20 cycles before PIV measurements began. In most cases, 12 image pairs for each

of 200 cycles were acquired. In the ten runs conducted the parameter  $\gamma$  varied from 0.8 to 2.0 (Table 1).

Table 1. Summary of experimental parameters.

Case	$\alpha$	$\beta$	$\omega$ (rad/s)	$N$ (rad/s)	$\gamma$
1	12.1	15.0	0.161	0.772	0.808
2	15.0	15.0	0.264	1.021	1.000
3	14.9	15.0	0.192	0.746	0.995
4	18.0	15.0	0.229	0.742	1.194
5	22.9	15.0	0.314	0.808	1.502
6	27.8	15.0	0.358	0.767	1.802
7	31.2	15.0	0.382	0.736	2.003
8	30.0	30.0	0.321	0.641	1.000
9	37.0	30.0	0.417	0.691	1.204
10*	15.0	15.0	0.205	0.793	0.999

## CHAPTER 3. RESULTS AND DISCUSSION

### A. Properties of the Incident Wave

The salinity measured at a fixed point in the wave beam oscillates mainly at the frequency  $\omega$ . Ideally the wave would be sinusoidal. In Cases 5, 7 and 9, the wave form is nearly sinusoidal (Fig. 7), while in Cases 6 and 10 the waves were distorted a bit possibly due to slight mechanical jamming of the wavemaker. The upward tilt of the waveform in Cases 6 and 8 could indicate that the waves were part of a wave group. In all cases the dominant frequency is close to the wavemaker frequency.

The horizontal wavelength ranged from 0.4 to 0.6 m, and the vertical wavelength was about 0.13 m (Table 2). These lengths were determined from velocity sections measured perpendicular to the incoming wave beam (Fig. 8). In Case 3, for example, the wavelength was easier to determine, but in other cases, such as Case 2, determining the wavelength was more difficult because the velocity magnitudes were not as equally distributed as in Case 3. The wavelength perpendicular to the wave beam varied from 11 to 14 cm, or about 45-55% of the height of the wavemaker stack.

The amplitudes of the waves were small. The height  $S_0$  of the salinity signal varied from 0.003% to 0.03% (Fig. 7), and the isotherm displacement  $\zeta_0$ , defined as

Table 2. Wavelengths and boundary layer thicknesses in four of the experimental cases.

Case	$\lambda_x$ (m)	$\lambda_z$ (m)	$k$ ( $\text{m}^{-1}$ )	$m$ ( $\text{m}^{-1}$ )	$h$ (mm)		$h_{meas}/h_{pred}$
					Measured	Predicted	
1	0.606	0.130	10.36	48.46	12	14.2	0.84
2	0.490	0.131	12.82	47.86	18	14.6	1.23
3	0.492	0.131	12.77	47.92	18	14.6	1.23
4	0.413	0.134	15.22	46.83	12	15.2	0.79

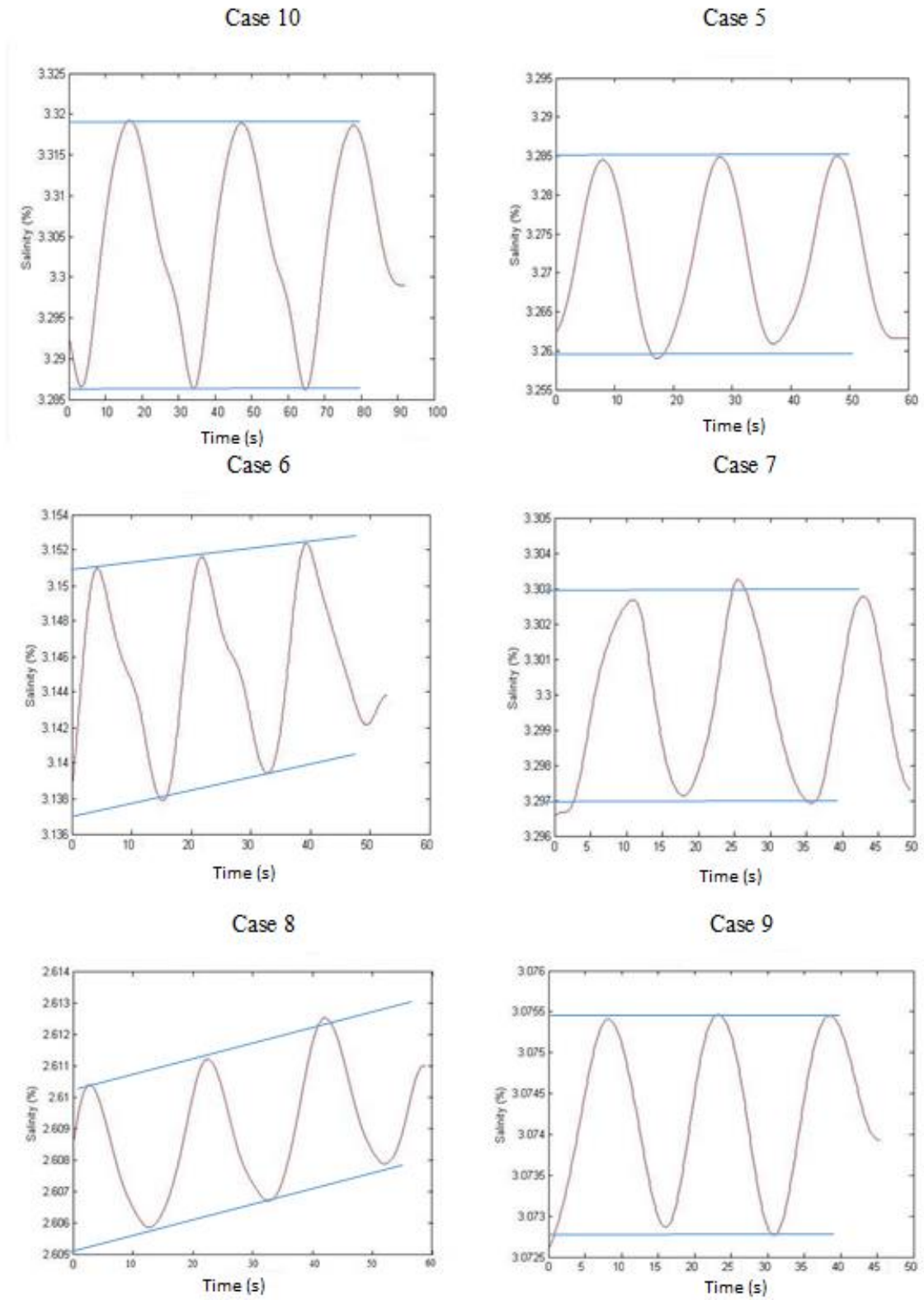
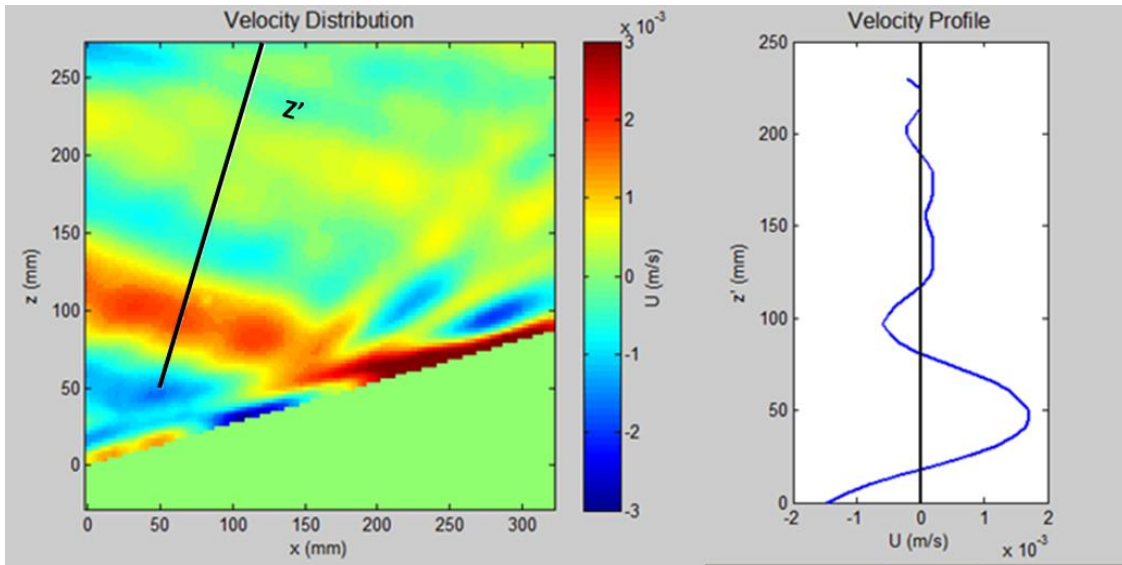


Fig. 7. Salinity signals measured by the MSCTI at a fixed point.

$$\zeta_0 = \frac{S_0/2}{d\bar{S}/dz} \quad (11)$$

where  $d\bar{S}/dz$  is the background salinity gradient, varied from 0.2 mm to 3 mm (Table 3).

Case 2



Case 3

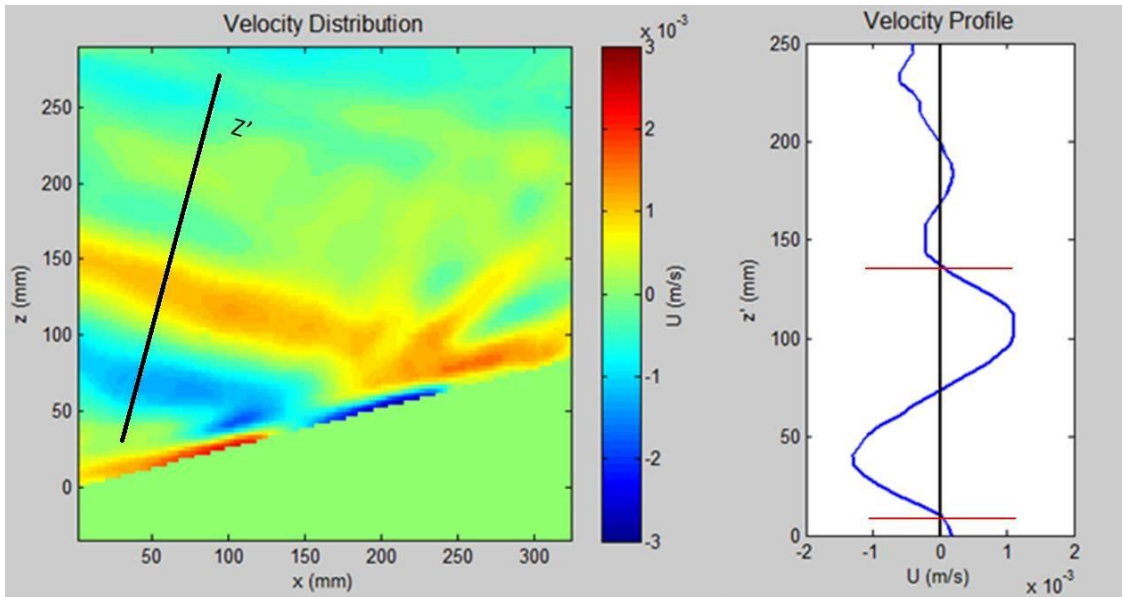


Fig. 8. Wavelength determination from velocity fields of PIV.

Dimensional analysis shows that  $\zeta_0/A = f(\omega/N)$ , where  $A$  is the amplitude of the wavemaker, and the measurements show that  $\zeta_0/A$  decreases as  $\omega/N$  increases (Fig. 9).

Table 3. Wave amplitudes for six of the experimental cases. The wavemaker amplitude  $A$  was 0.01 m in all cases.

Case	$\omega/N$	$\zeta_0$ (m)	$\zeta_0/A$
10	0.259	0.00255	0.251
5	0.389	0.00185	0.182
6	0.467	0.00103	0.102
7	0.519	0.00046	0.045
8	0.501	0.00056	0.055
9	0.603	0.00024	0.024

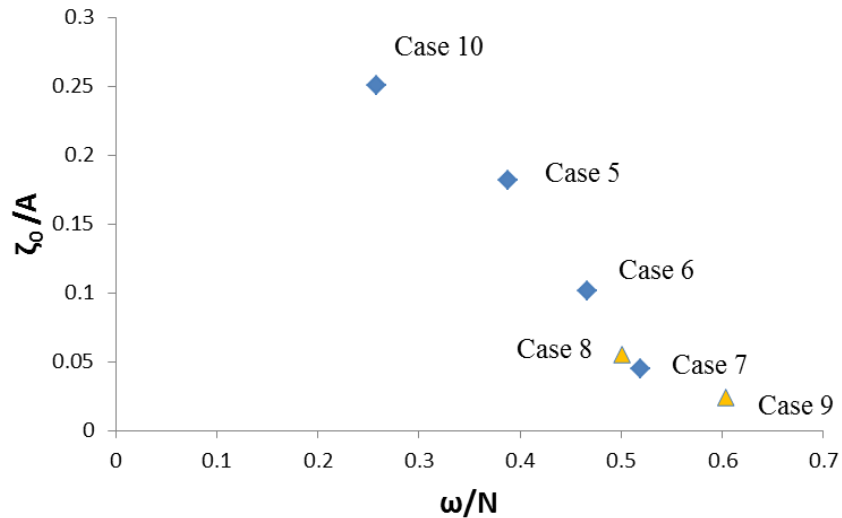


Fig. 9. Negative correlation between  $\zeta_0/A$  and  $\omega/N$ . The diamonds and triangles represent the results on the 15° and 30° slope respectively.



The Froude numbers of the incident waves were large enough to lead to turbulence. Chalamalla et al. (2013) determined that values of the Froude number, defined as

$$Fr = \frac{U_0 k}{\omega} \quad (12)$$

where  $U_0$  is the amplitude of the incident wave velocity in the  $x$ -direction, greater than about 0.05 lead to instability and turbulence in the reflected wave. For Cases 1 to 4, the Froude number exceeded 0.06. Therefore, turbulence should occur after the wave reflects from the sloping boundary.

## B. Velocity Fields

As expected from theory, the primary reflection from the slope depends on  $\gamma$  (Fig. 10). In the only subcritical case (Case 1), no reflection can be seen. In the supercritical cases (Cases 4-7, 9), forward reflection occurs, but it is more difficult to detect in the velocity fields when the value of  $\gamma$  is only slightly supercritical (e.g., Case 4). In the critical cases (Cases 2, 3, 8), the reflection occurs along the slope.

Another significant phenomenon observed is the presence of harmonics when  $\gamma \geq 1$ . The harmonics propagate at an angle given by

$$\theta_n = \sin^{-1}(n \sin \alpha) \quad (13)$$

(Gostiaux et al. 2006) where  $\theta_n$  is the propagating angle of the  $n$ th harmonic. For example, the angles of the second and third harmonics in critical cases— $\theta_2 = 31 \pm 1^\circ$  and  $\theta_3 = 51 \pm 1^\circ$ —are shown for Cases 2 and 3 in Fig. 10, and they match well with the observations. In Case 8, in which  $\alpha = 30^\circ$ , the second harmonic propagates vertically (i.e.,  $\theta_2 = 90^\circ$ ). This harmonic is nearly evanescent; that is, its energy decays with distance from the generation region. Therefore, the second harmonic is difficult to see in Case 8.

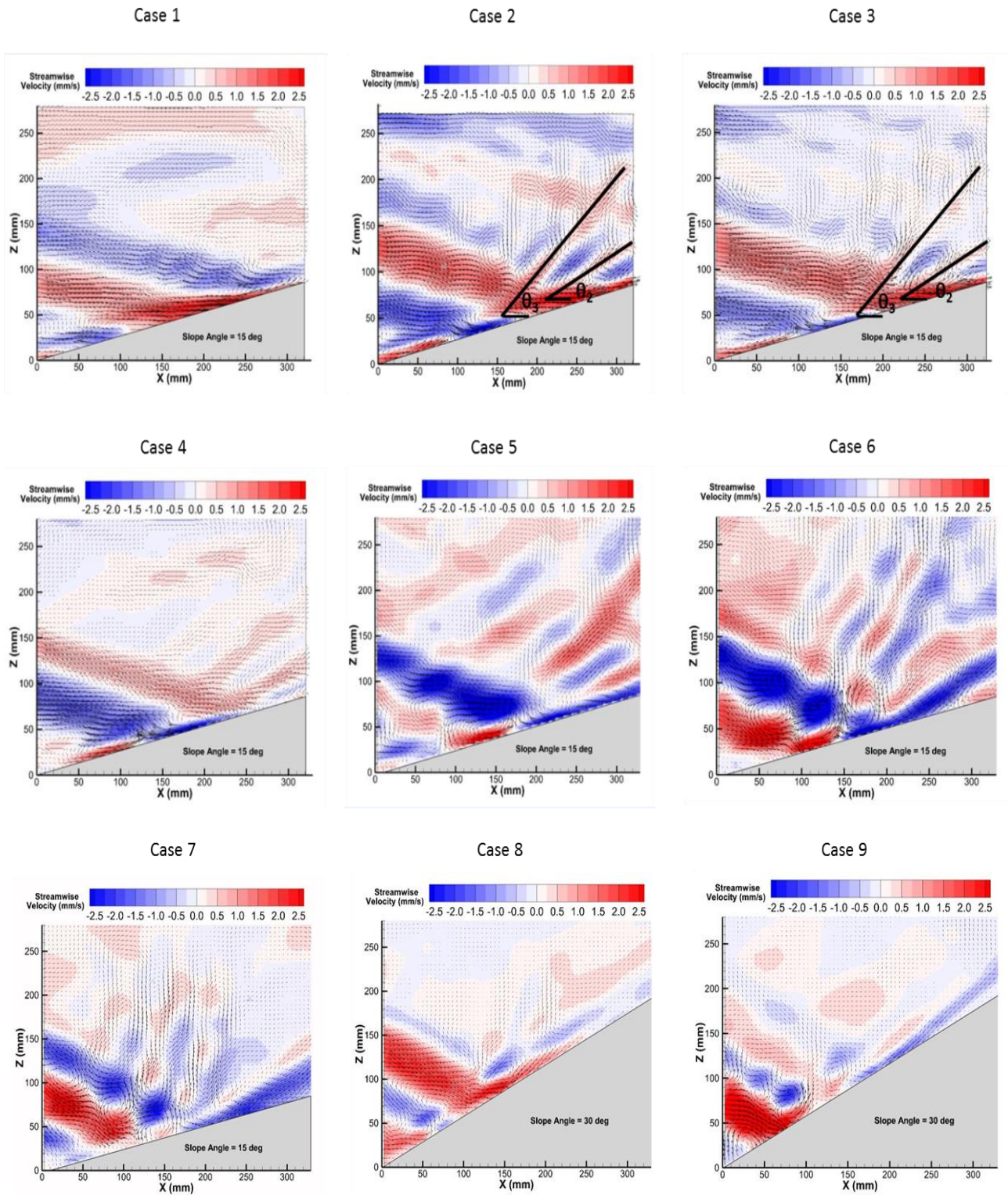


Fig. 10. Velocity fields from PIV.

### C. Dissipation Fields

The dissipation was largest near the slope, and it was patchily distributed. For example, in Case 2 (Fig. 11), the dissipation reached peak values between  $10^{-7}$  and  $10^{-6} \text{ m}^2/\text{s}^3$  in a layer of about 20 mm thickness near the slope. Outside the layer, the dissipation dropped sharply to background levels, at least in the critical cases. The higher values of dissipation were not distributed uniformly along the slope. Instead, they occurred in patches with along-slope lengths varying between 25 and 75 mm. These patches appeared to move up the slope as the phase increased. The line of dissipation values near  $2 \times 10^{-8} \text{ m}^2/\text{s}^3$  just above the patches is probably due to a reflection of the light sheet from the slope in the PIV images (Fig. 12).

When  $\gamma$  increases, high values of dissipation still occur in patches along the slope, but elevated values also occur away from the slope (Fig. 13). For all values of  $\gamma$  between 1.2 and 2.0, the highest dissipation values were still found mostly along the slope, but values between  $10^{-8}$  and  $10^{-7} \text{ m}^2/\text{s}^3$  appeared in the zones with reflecting waves and harmonics. The dissipation along the primary reflection was about 10 times larger than the dissipation along the harmonics. A curious aspect of Cases 6 and 7 and—to some extent—Case 5 is the high value of dissipation on the incoming wave, before reflection occurs. The values of dissipation in the incoming wave increase as  $\gamma$  increases. These phenomena are observed in Cases 8 and 9, which had a steeper slope ( $\beta = 30^\circ$ ), but in those cases high values of dissipation in the incoming wave appear at lower  $\gamma$  (Fig. 14).

Three cases with critical reflection (Cases 2, 3, 8) were run to explore the effect of various parameters on the dissipation. The case with a steeper slope (Case 8,  $\beta = 30^\circ$ ) has

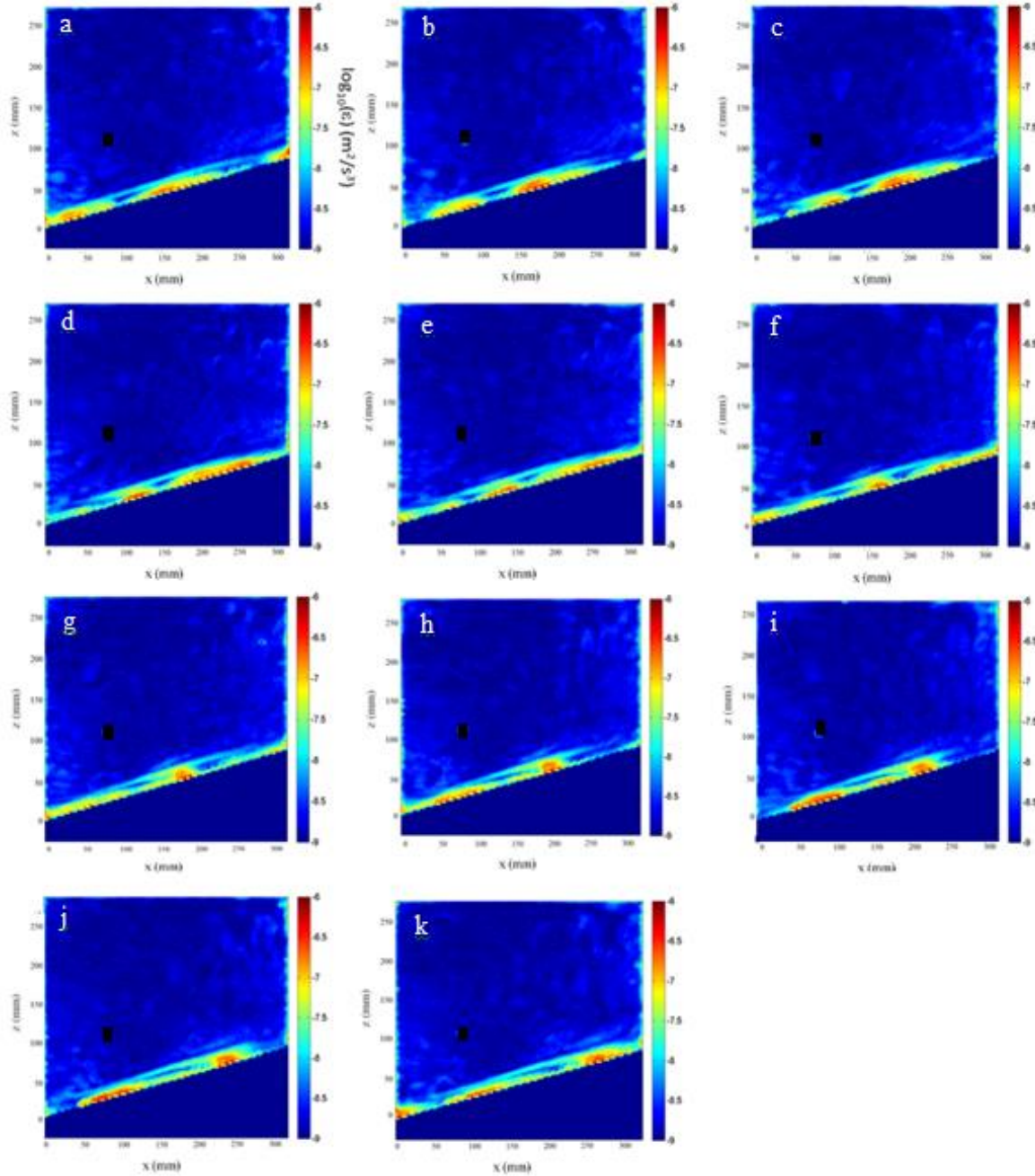


Fig. 11. 2D dissipation distribution in Case 2. Panels a-k correspond to phases 1-11. A bad point due to the damage of lens was blocked from the dissipation field.





Fig. 12. PIV image showing the reflection of the light sheet (circled).

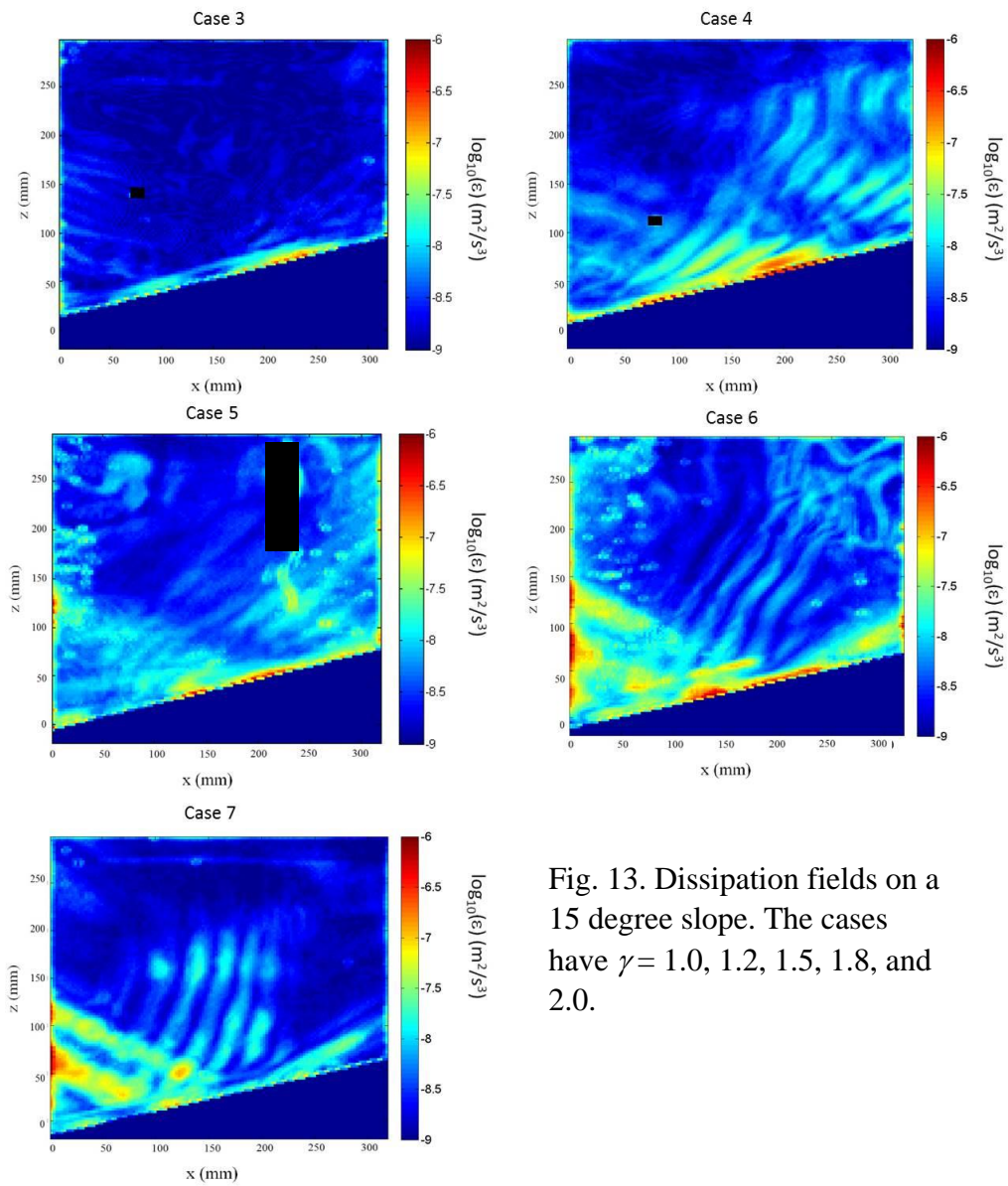


Fig. 13. Dissipation fields on a 15 degree slope. The cases have  $\gamma = 1.0, 1.2, 1.5, 1.8,$  and  $2.0$ .

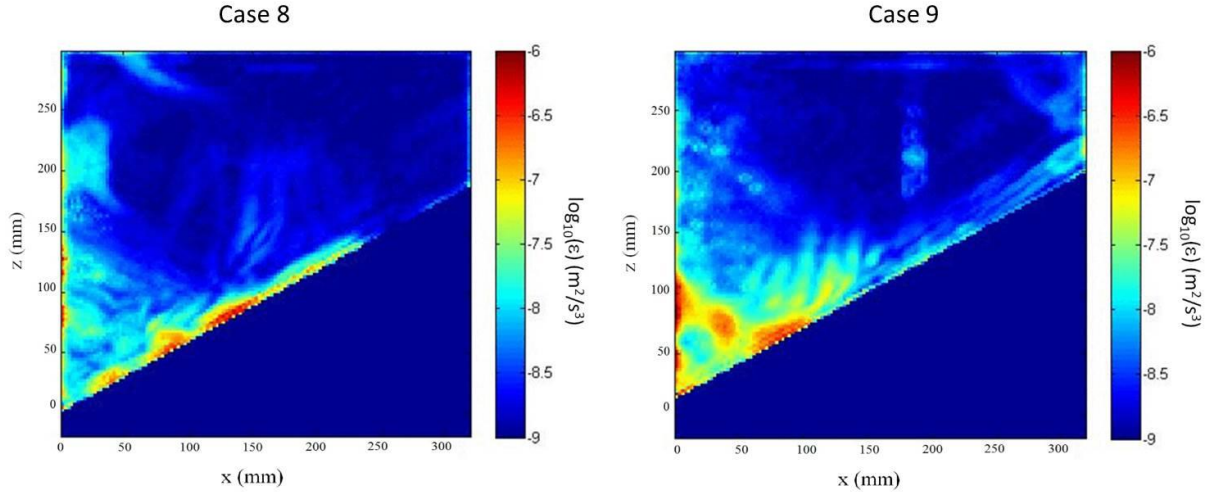


Fig. 14. Dissipation fields on a  $30^\circ$  slope. Case 8:  $\gamma = 1.0$ , Case 9:  $\gamma = 1.2$ .

larger dissipation concentrated in shorter patches than in Case 3 ( $\beta = 15^\circ$ ), as shown in Fig. 15. Case 2, which has a larger wave frequency and buoyancy frequency than Case 3, also has larger dissipation near the slope (Fig. 16). These observations are partly consistent with the theoretical estimates of dissipation of Ivey et al. (2000). Considering energy flux and dissipation in the boundary layer, they proposed that the cycle-averaged dissipation is

$$\bar{\epsilon} = 0.4(1-r)w_0^2 N \cos \alpha \sin 2(\alpha + \beta) \quad (14)$$

where  $r$  is a reflection coefficient (assumed to be near zero for critical reflection) and  $w_0$  is the maximum particle speed. Equation (14) suggests that the dissipation should be about 2-3 times higher in Case 2 than in Case 3, which is qualitatively consistent with observations. However, it also suggests that the dissipation in Case 8 should be about 10 times smaller than in Case 3, which differs from the observations.

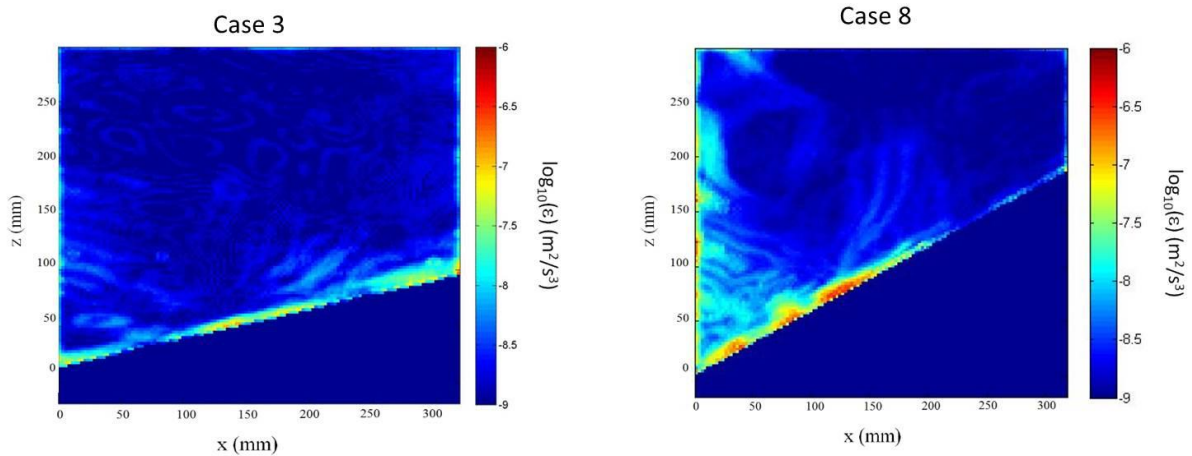


Fig. 15. Comparison of dissipation fields in cases with different slope. Case 3:  $\beta = 15^\circ$ ; Case 8:  $\beta = 30^\circ$ .

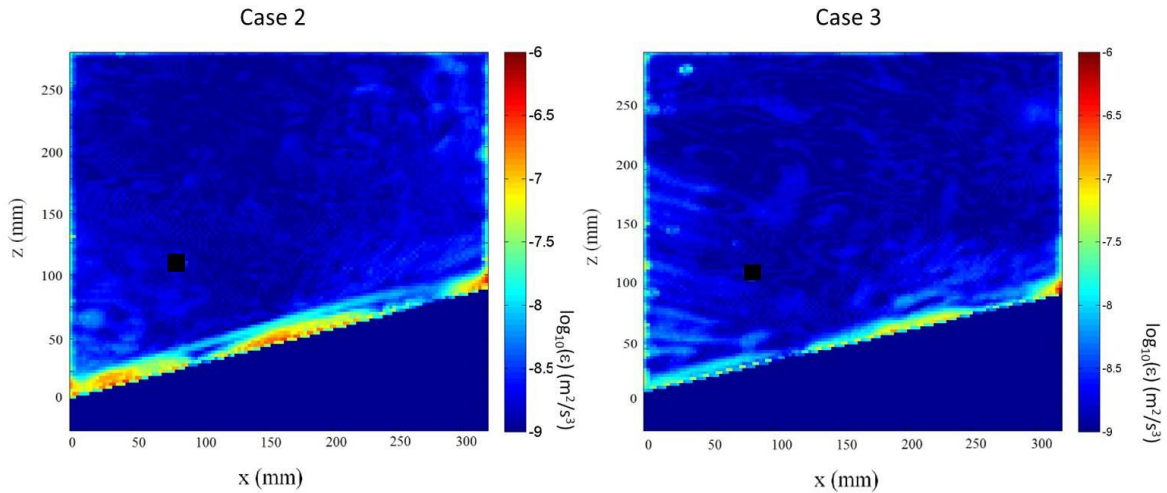


Fig. 16. Comparison of dissipation fields in cases with different wave frequency and buoyancy frequency. Case 2:  $\omega = 0.264$  rad/s,  $N = 1.021$  rad/s; Case 3:  $\omega = 0.192$  rad/s,  $N = 0.746$  rad/s

The large dissipation near the slope and sharp decrease away from the slope was also observed in previous work. A profile of dissipation as a function of distance perpendicular to the slope in Case 2 shows a decrease of about two orders of magnitude in 20 mm (Fig. 17). Lorke's (2007) long-term measurements with acoustic profilers in Lake Überlingen showed a similar sharp decrease: The near-bottom dissipation was about 100 times larger than in Case 2, but it still dropped by about two orders of magnitude in 0.2 m (fig. 8 of Lorke 2007). Ivey

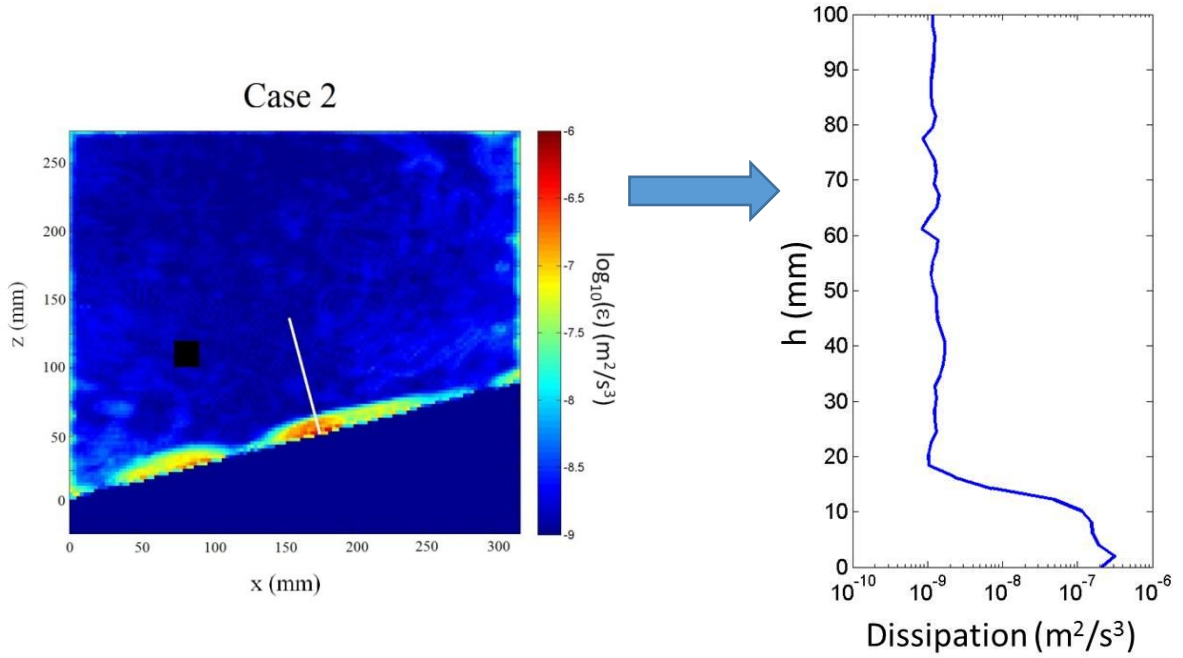


Fig. 17. Profile of dissipation in Case 2.

et al. (2000) moved the Portable Flux Profiler through the boundary layer of thickness  $h$  and observed a similar decrease of about two orders of magnitude. The measurements from the present experiments add to the previous laboratory and field measurements by illustrating how the dissipation varies along the slope as well as perpendicular to the slope.

The measured thickness of the boundary layer is consistent with the predictions of Ivey et al. (2000). The measured thickness in Cases 1-4 was between 12 and 18 mm (Table 2); larger values occurred for critical reflection. Ivey et al. (1995) modeled the boundary layer thickness as 10-15% of the wavelength of the incident wave perpendicular to the slope, and Ivey et al. (2000) used this result and geometry to predict

$$h = 0.1 \frac{2\pi}{\sqrt{k^2 + m^2} \cos(\alpha + \beta)} \quad (15)$$



The measured values are within about 20-25% of the predictions from equation (15) (Fig. 18). This agreement is reasonable given that the coefficient in equation (15) has about 50% uncertainty.

The results from the current laboratory experiments resemble results from the direct numerical simulations (DNS) of Chalamalla et al. (2013). As in the experiments, the dissipation was largest near the slope, and it occurred in patches in the DNS. The DNS also showed that regions of high dissipation coincided with regions of overturning in the density field and regions of high turbulent kinetic energy (Fig. 7 of Chalamalla et al. 2013). The correspondence between TKE and dissipation occurs in the laboratory experiments as well (Fig. 19). In a critical case (Case 2), the patches of high values of both TKE and dissipation are confined to a thin layer near the slope, but in a supercritical case (Case 4), high values of

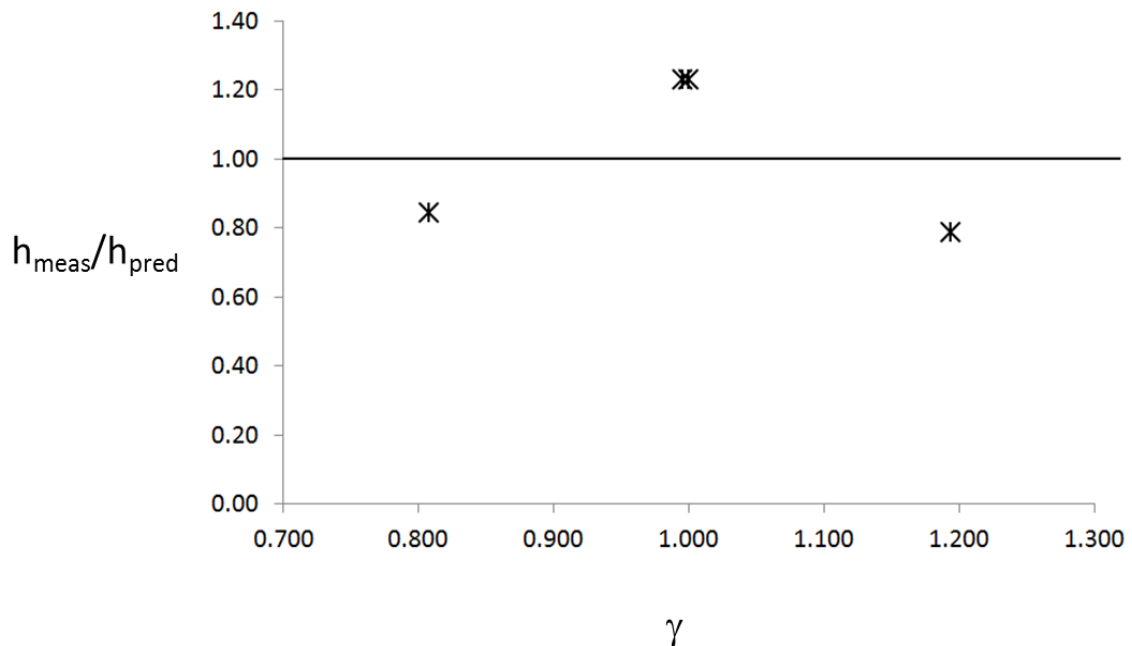


Fig. 18. Comparison of measured and predicted boundary layer thicknesses.

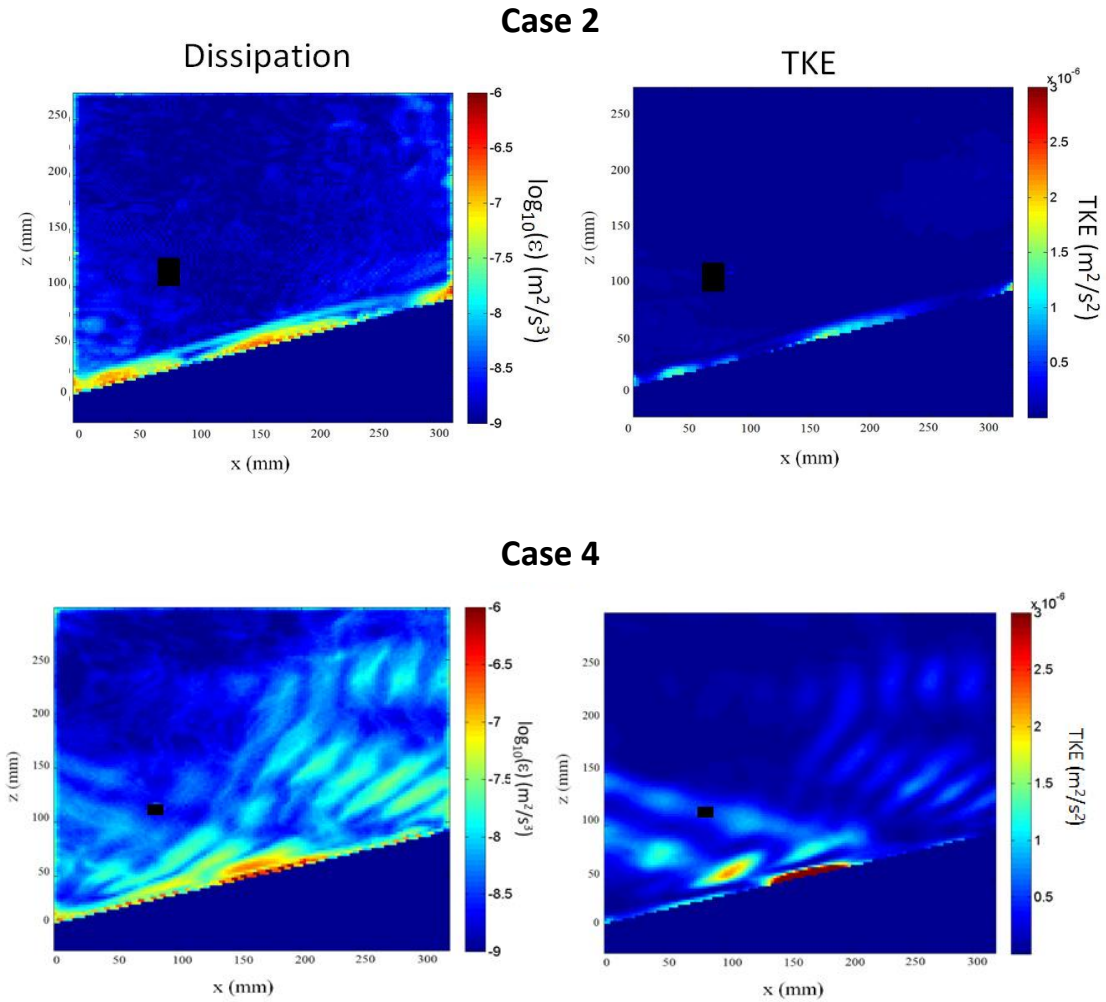


Fig. 19. The comparison of dissipation with TKE.

TKE also appear in the harmonics.

Although the dissipation can reach large values in particular regions, spatially averaged values of dissipation are much lower. In all cases maximum values of dissipation are  $O(10^{-6})$   $\text{m}^2/\text{s}^3$  in patches along the slope, but dissipation outside these patches can be much smaller. As in the theory of Ivey et al. (2000), the dissipation was spatially averaged over a box along the slope, centered on the impinging point of the incident wave; the box's height was  $h$  and the length was

$$\ell = \frac{2\pi \sin \alpha}{k \sin(\alpha + \beta)} \quad (16)$$

The spatially-averaged dissipation is about two orders of magnitude smaller than the maximum dissipation: In Case 3, the maximum averaged dissipation was  $5.6 \times 10^{-9} \text{ m}^2/\text{s}^3$ , while in Case 9, the maximum was  $2.2 \times 10^{-9} \text{ m}^2/\text{s}^3$ . In most cases, the averaged dissipation varied with phase, but the ranges differed. For example, values in Case 3 vary by a factor of 3, while values in Case 9 vary by less than a factor of 2 (Fig. 20). The cycle-averaged dissipation ranged from  $10^{-9} \text{ m}^2/\text{s}^3$  in Case 8 to  $10^{-8} \text{ m}^2/\text{s}^3$  in Case 4.

#### D. Implications for mixing

Values of the dimensionless dissipation, expressed as the parameter  $\varepsilon/\nu N^2$ , are small. This parameter is used in oceanographic and limnological studies to characterize the intensity of the turbulence. With a maximum dissipation of  $O(10^{-6}) \text{ m}^2/\text{s}^3$  and a buoyancy frequency of  $O(1) \text{ rad/s}$ , the maximum value of  $\varepsilon/\nu N^2$  is  $O(1)$ . This value is comparable to those in the

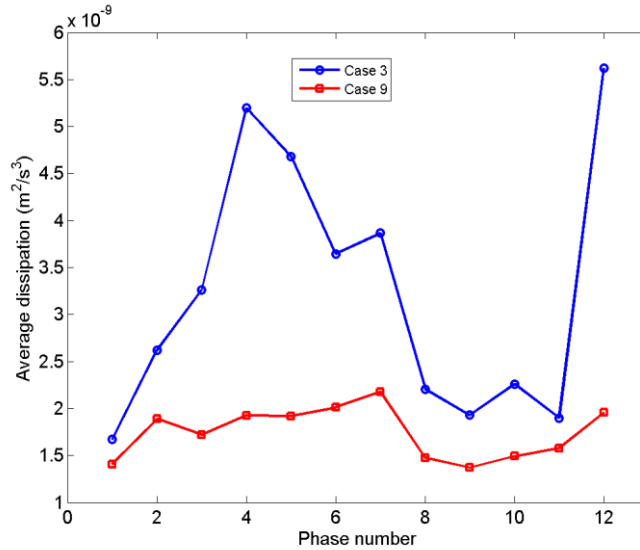


Fig. 20. Spatially-averaged dissipation as a function of phase for two example cases.

laboratory experiments of Ivey et al. (2000), in which  $\varepsilon/\nu N^2 \approx 1$ , and the DNS of Chalamalla et al. (2013), in which  $\varepsilon/\nu N^2 \approx 5$ . However,  $\varepsilon/\nu N^2 = O(1) \text{ m}^2/\text{s}^3$  is small compared to observations in most natural flows, as shown by the compilation of Jackson and Rehmann (2014). For example, in an Arctic fjord  $\varepsilon/\nu N^2$  was between 30 and 6000, and in the Equatorial Undercurrent and Hawaiian ridge,  $\varepsilon/\nu N^2$  ranged from about 10 to over  $10^5$ . Values of  $\varepsilon/\nu N^2$  of  $O(1) \text{ m}^2/\text{s}^3$  are relevant for boundary mixing in lakes and shelves, however, since measurements of the metalimnion of lakes yield  $0.05 < \varepsilon/\nu N^2 < 7000$  (Saggio and Imberger 2001, Etemad-Shahidi and Imberger 2001) and measurements on the Black Sea shelf yield  $0.07 < \varepsilon/\nu N^2 < 80$  (Lozovatsky and Fernando 2002).

Even though  $\varepsilon/\nu N^2$  is small, significant mixing might occur. Many researchers, following the work of Gibson (1980), argued that active turbulence would be extinguished when  $\varepsilon/\nu N^2$  fell below a certain transition value, usually between 15 and 30. In this case, the eddy diffusivity of salinity  $K_S$  would be equal to the molecular diffusivity of salinity  $D_S$ . However, the model developed by Ivey et al. (2000) to predict the eddy diffusivity gives different results: For length scales between the Batchelor scale and Kolmogorov scale, it predicts

$$\frac{K_S}{D_S} \sim Sc \frac{\varepsilon}{\nu N^2} \quad (17)$$

where  $Sc = \nu/D_S$  is the Schmidt number. With  $Sc \approx 700$  for salt, values of  $\varepsilon/\nu N^2$  of  $O(1)$  would give eddy diffusivities  $O(10^3)$  times larger than the molecular diffusivity of salt.

As noted in the previous subsection, while maximum values of dissipation reach  $O(10^{-6}) \text{ m}^2/\text{s}^3$ , the averaged values of dissipation were much smaller. Because the dissipation in the boundary layer is patchy, values of  $\varepsilon/\nu N^2$  based on cycle-averaged dissipation ranged

between 0.01 and 0.2. Equation (17) then gives  $6 \times 10^{-9} < K_S < 1.8 \times 10^{-7} \text{ m}^2/\text{s}$ , and the standard diffusion estimate  $(K_S t)^{1/2}$  would give a mixed region near the boundary of between 0.4 and 3 cm after 200 wave cycles. Density profiles measured after the wavemaker was turned off in Cases 2 and 4 showed no mixed layer near the bottom.

## CHAPTER 4. CONCLUSIONS

Velocity fields for internal waves impinging on a sloping boundary were measured with particle image velocimetry (PIV) and used to derive two-dimensional fields of dissipation. Velocities were acquired over 200 wave cycles at 12 phases per cycle. These measurements allowed the calculation of phase-averaged velocity and dissipation fields. Significant findings included the following:

- 1) Harmonics were observed in the velocity fields in some cases with  $\gamma \geq 1$ , and the angle of the harmonics agreed with the theory of Gostiaux et al. (2006).
- 2) The highest dissipation was patchily distributed near the slope, and it formed a layer whose thickness was within 20-25% of the values predicted by the work of Ivey et al. (2000). The sharp drop in dissipation was similar to that observed in the field measurements of Lorke (2007).
- 3) For supercritical condition ( $\gamma > 1$ ), high values of dissipation were not confined solely in a layer near the slope. The high dissipation also appeared in regions with reflecting waves, harmonics, and—in some cases—the incident waves.
- 4) A comparison of critical cases showed that differences in measurements between cases with slope angle of  $15^\circ$  were qualitatively consistent with an expression for predicting the cycle-averaged dissipation (Ivey et al. 2000), although a comparison of cases with different slope angles was not.
- 5) As in the direct numerical simulations of Chalamalla et al. (2013), regions of high turbulent kinetic energy coincided with regions of high dissipation for all cases.

- 6) Values of  $\varepsilon/\nu N^2$  were small near the slope. Maximum values were  $O(1)$ , while values based on cycle-averaged dissipation were less than 0.2. In these cases, the patchy nature of the dissipation suggests that little mixing will occur.

Future work could include using molecular tagging techniques to measure fields of velocity and scalars. It could compare the accuracy of velocities measured with PIV and molecular tagging, and once molecular tagging is extended to salt-stratified flows, it could produce fields of density fluxes so that mixing can be measured directly. The combination of velocity, turbulence, and flux measurements would allow mixing parameterizations commonly used in oceanography and limnology to be tested.

## APPENDIX A. WAVEMAKER NOTES

The purpose of the wavemaker is to generate the monochromatic oscillation in stratified flow so that the internal waves can be excited. The model of the wavemaker is based on Gostiaux et al. (2006). The basic configuration of the wavemaker adopted a major shaft to string the eccentric gears together; a round of secondary shafts were used to set the angle for gear to gear so that the gear stack can drive the plates moving at 12 phases. The eccentricity ratio of gears is 1 cm which determines the amplitude of wavemaker  $A$ . Since the eccentricity cannot be changed after the wavemaker is built,  $A = 1$  cm was constant for all experimental cases.

The cross-beam wavelength is related to the height of gear stack and fluid properties. In the initial design, the stack was composed of 12 eccentric gears. However the height of the stack was too large (25.3 cm) so that the wavemaker impinging point was hard to contain in the PIV viewing window, especially when the window size needs to be small enough so that dissipation can be resolved. Therefore the gear stack had to be reassembled; five gears were taken out and the angle between gears was adjusted to  $65.47^\circ$ , and then the height of the gear stack was shortened to 58% of the original height. After reassembling the wavemaker the impinging area can be observed in an identified PIV window.

The motor selection mainly depends on the friction of the wavemaker components, especially between the gear stack and plates as well as plates and the lateral slotted plates. The waterproof foam board called RenShape dramatically reduced mechanical friction between parts. Because the wavemaker oscillated at low frequency, a high-torque gear needs motor was needed to drive it. A system of gears was built in the gear motor to enlarge the output torque. Therefore a gear motor with the gear ratio of 36:1 and holding torque of 3.95



N-m (560 oz-in) was applied to drive the wavemaker. Also, the gear motor was controlled by a motor driver which can be easily manipulated through the computer interface program, Si Programmer ®.

## APPENDIX B. MSCTI PROBE & CALIBRATION

The salinity measurements are accomplished by applying a high-accuracy Model MicroScale Conductivity-Temperature Instrument (MSCTI) system. The Model 125 MSCTI probe is composed of high-resolution thermistor and a conductivity sensor, and it also comes with an electronic bridge which allows one to adjust the range and precision of measurements. The MSCTI is able to obtain the temperature and electrical conductivity of water containing conductive ions at the same time and output analog voltages as functions of temperature and electrical conductivity (Fig. B.1). Then temperature and electrical conductivity can be used to compute salinity. During the experiments the MSCTI probe has two functions: the internal wave can be measured at a fixed point, or the salinity profile can be measured by vertically moving the probe at a constant speed. In our case, the electro-mechanical assembly UniSlide® was used to drive the MSCTI. More specifications of the MSCTI are listed in Table B.1.

The calibration divides into two steps: calibration of the thermistor and calibration of the conductivity sensor. Before the calibration, the electrical bridge inherent voltage was recorded to be used in the response equation later. First, the probe was disconnected from the electrical bridge. Then the electrical bridge was turned on, and the voltages at the temperature and conductivity outputs were measured and recorded them as  $V_{\text{toff}}$  and  $V_{\text{coff}}$  (Fig. B.2).

A digital thermometer with an accuracy of  $0.002^{\circ}\text{C}$ , a Plexiglas tank and an immersion circulator were used to accomplish the thermistor calibration. Once the Plexiglas tank was filled with water of room temperature, the probe and thermometer were put in the water at the same location to guarantee the measurements from probe and thermometer

coincide. Then the immersion circulator was used to heat up the water slowly, and the voltage and the temperature were recorded at regular intervals. When the water temperature reached the upper limit of the experimental range, the immersion circulator was turned off.

The voltage from the thermistor was used to compute temperature with

Table B.1. MSCTI specifications (PME 2008).

TEMPERATURE	
Measurement equation	$V_o = G \exp(A+B/T) + V_{off}$
8 hour calibration stability	Better than 0.01 deg C
Time response	Approx. 7E-3 seconds
Noise	< 1mV RMS 10 Hz to 200 Hz
Output voltage range	+/- 5 volts
Temperature range	-10 to 100 deg C

CONDUCTIVITY	
Measurement equation	$V_o = G * C + V_{off}$
8 hour calibration stability	Better than 1% of C reading
Time response	-3db at approx. 800 hz
Spatial response	-3db at approx. 4 cyc/cm
Noise	< 1mV RMS 10 Hz to 1 kHz
Output voltage range	+/- 5 volts
Linear conductivity range	0.5 to 800 mS/cm

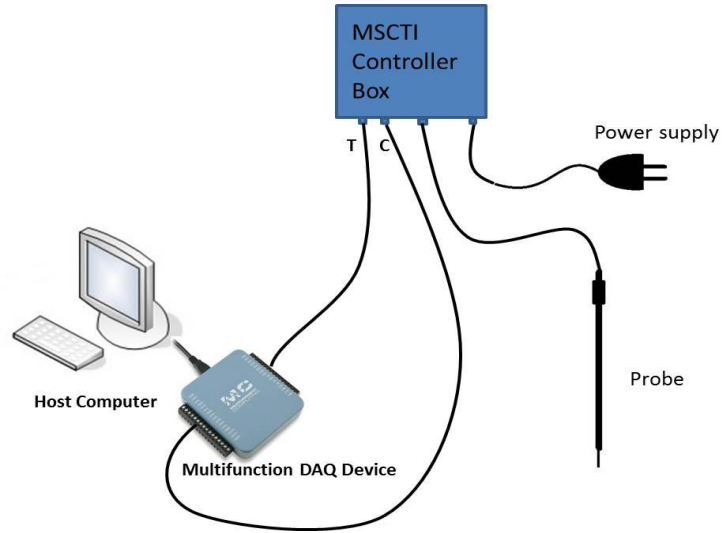
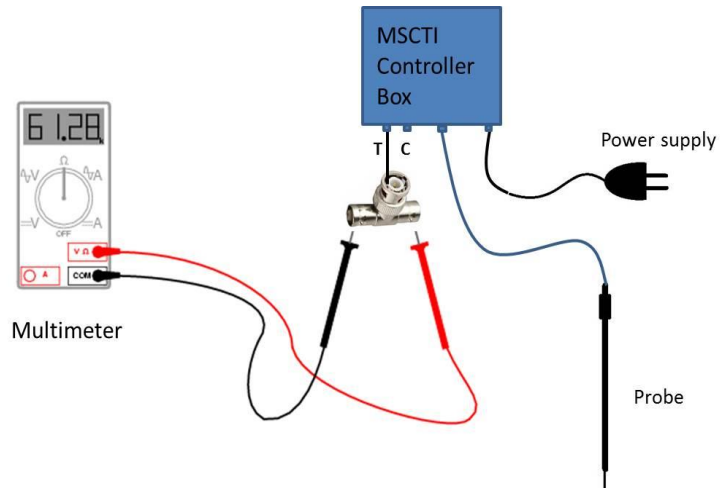


Fig. B.1.MSCTI configuration.

Fig. B.2.MSCTI calibration for  $V_{Toff}$  and  $V_{Coff}$ .

$$y = C_1x + C_2 \quad (B.1)$$

where

$$y = \frac{1}{T} \quad (B.2)$$

$$x = \ln\left(1 - \frac{V_T}{V_{Toff}}\right) \quad (B.3)$$

and  $T$  is in Kelvin and  $C_1$  and  $C_2$  are calibration coefficients (1/K) found using a least squares fit. The coefficients were recorded and entered into the LabVIEW sampling program where the temperature voltage can be converted to the actual temperature.

The calibration of the conductivity sensor used solutions with known salinity to correlate conductivity from MSCTI. Prior to the calibration, five solutions were made within the expected experimental range and the necessary amount of salt and water was calculated from the definition of salinity:

$$S = \frac{m_{salt}}{m_{salt} + m_{water}} \times 100 \quad (\text{B.4})$$

where  $S$  is salinity in % and  $m_{salt}$  and  $m_{water}$  represent the mass of salt and water, respectively. The conductivity voltage and solution temperature were recorded at the same time. Then the conductivity was converted by the input of corresponding solution temperature and salinity in MATLAB code. The voltage and conductivity obey

$$V_C = G_C \sigma + V_{Coff} \quad (\text{B.5})$$

where  $V_C$  is the voltage output from probe,  $\sigma$  is the conductivity (mS/cm) and  $G_C$  is another coefficient, sensor gain, which is inputted in the LabVIEW sampling program to internally convert the conductivity voltage to conductivity. By plotting the linear relation of  $V_C$  and  $\sigma$ ,  $G_C$  was obtained.

An example of the curve of the response equation is shown in Figures B.3 and B.4.

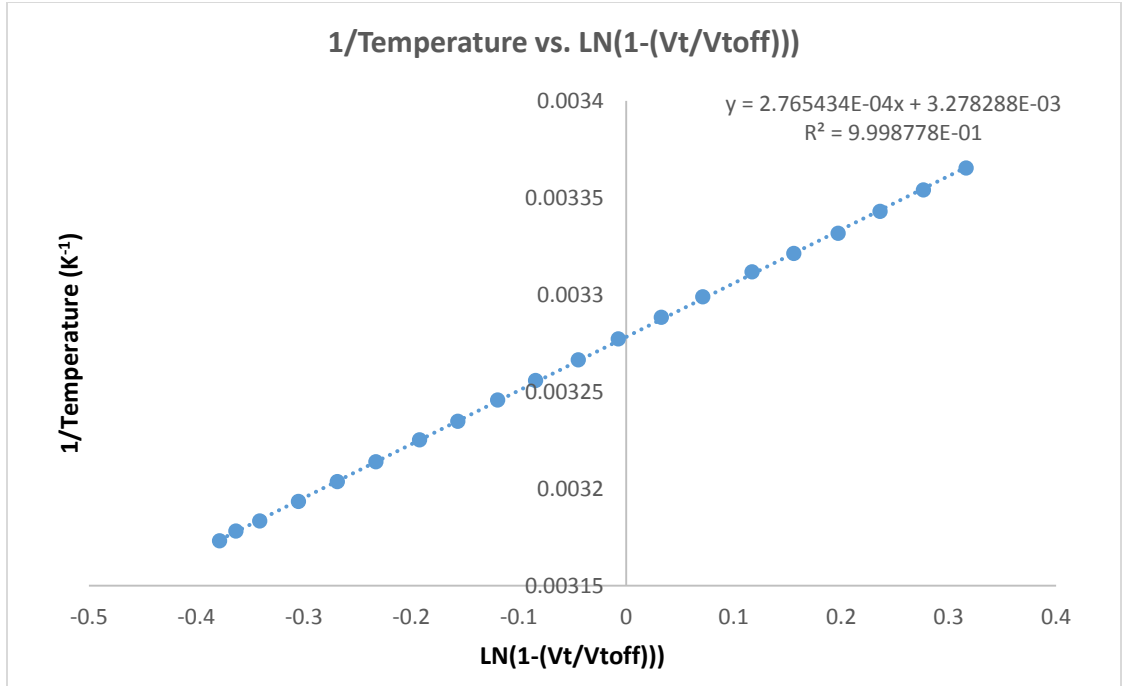


Fig. B.3. Curve of response equation B.1,  $C_1 = 2.765 \times 10^{-4} \text{ K}^{-1}$  and  $C_2 = 3.28 \times 10^{-3} \text{ K}^{-1}$

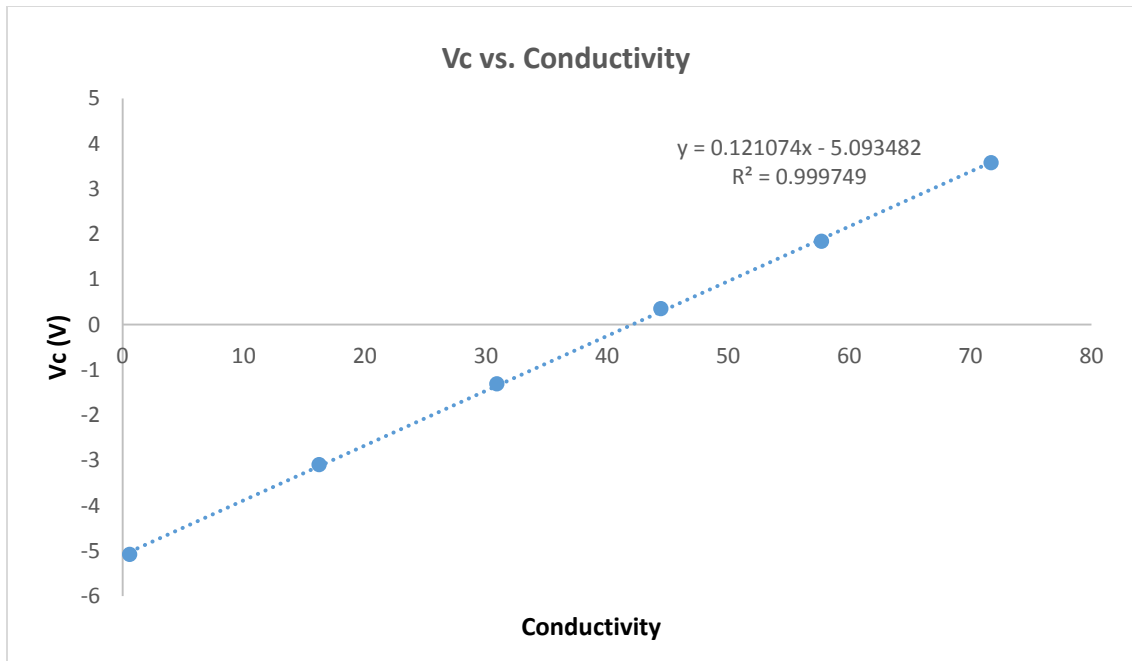


Fig. B.4. Curve of response equation B.5,  $G_C = 0.12 \text{ V}/(\text{mS}/\text{cm})$ .

## REFERENCES

- Cacchione, D. A., Pratson, L. F., and Ogston, A. S. (2002). "The shaping of continental slopes by internal tides." *Science*, 296(5568), 724-727.
- Chalamalla, V. K., Gayen, B., Scotti, A., & Sarkar, S. (2013). Turbulence during the reflection of internal gravity waves at critical and near-critical slopes. *Journal of Fluid Mechanics*, 729, 47–68. doi:10.1017/jfm.2013.240
- Etemad-Shahidi, A., and Imberger, J. (2001). "Anatomy of turbulence in thermally stratified lakes." *Limnol. Oceanogr.*, 46(5), 1158-1170.
- Fortuin, J., 1960: Theory and application of two supplementary methods of constructing density gradient columns. *J. Polym. Sci.*, 44, 505–515.
- George, W. K., and Hussein, H. J. (1991). "Locally axisymmetric turbulence." *J. Fluid Mech.*, 233, 1-23.
- Gibson, C. H. (1980). "Fossil temperature, salinity and vorticity in the Ocean. In *Marine Turbulence* (ed. J. C. T. Nihoul), p.221. Elsevier
- Gostiaux, L., Didelle, H., Mercier, S., & Dauxois, T. (2006). A novel internal waves generator. *Experiments in Fluids*, 42(1), 123–130. doi:10.1007/s00348-006-0225-7
- Gostiaux, L., Dauxois, T., Didelle, H., Sommeria, J., & Viboud, S. (2006). Quantitative laboratory observations of internal wave reflection on ascending slopes. *Physics of Fluids*, 18(5), 056602. doi:10.1063/1.2197528
- Hu, H., Yang, Z., & Sarkar, P. (2011). Dynamic wind loads and wake characteristics of a wind turbine model in an atmospheric boundary layer wind. *Experiments in Fluids*, 52(5), 1277–1294. doi:10.1007/s00348-011-1253-5
- Ivey, G. N., Winters, K. B., & De Silva, I. P. D. (2000). Turbulent mixing in a sloping benthic boundary layer energized by internal waves. *Journal of Fluid Mechanics*, 418, 59–76.
- Ivey, G.N., De Silva, I.P.D. & Imberger, J. 1995 Internal waves, bottom slopes and boundary mixing. Proc. Aha Huliko’a Hawaiian Winter Workshop on Topographic Effects in the Ocean. 199-205.
- Lorke, A. (2007). Boundary mixing in the thermocline of a large lake. *Journal of Geophysical Research*, 112(C9), C09019. doi:10.1029/2006JC004008
- Lozovatsky, I. D., and Fernando, H. J. S. (2002). "Mixing on a shallow shelf of the Black Sea." *J. Phys. Oceanogr.*, 32(3), 945-956.

- MacIntyre, S., Flynn, K. M., & Jellison, R. (1999). Boundary mixing and nutrient fluxes in Mono Lake, California, *44*(3), 512–529.
- McPhee-Shaw, E. E., & Kunze, E. (2002). Boundary layer intrusions from a sloping bottom: A mechanism for generating intermediate nepheloid layers, *107*, 1–16.
- Precision Measurements Engineering (2008). MicroScale Conductivity Temperature Instrument Model 125: Operator's Manual, Vista, CA.
- Raffel, M., Willert, C. E., Wereley, S. T., & Kompenhans, J. (2007). *Particle Image Velocimetry: A Practical Guide*, Springer, 448 pp.
- Rodenborn, B., Kiefer, D., Zhang, H. P., & Swinney, H. L. (2011). Harmonic generation by reflecting internal waves. *Physics of Fluids*, *23*(2), 026601. doi:10.1063/1.3553294
- Saarenrinne, P., & Piiro, M. (2000). Turbulent kinetic energy dissipation rate estimation from PIV velocity vector fields.
- Saggio, A., and Imberger, J. (2001). "Mixing and turbulent fluxes in the metalimnion of a stratified lake." *Limnol. Oceanogr.*, *46*(2), 392-409.

## ACKNOWLEDGMENTS

I would like to express my special appreciation to my major advisor Professor Dr. Chris Rehmann. Deeply thank you for offering me the opportunity of great value to work on this profound project. Thank you for as a very patient mentor to give me the careful guidance, useful comments and tremendous support of experimental setups, post processing, writing guide. I also particularly thank Dr. Hui Hu, Zhengyu Wang and Rye Waldman for supplying technical assistance on the experiment and PIV measurements. I would like to thank Dr. Roy Gu, Dr. Hui Hu and Dr. Chris Rehmann for serving as my committee members to give me valuable advice during every step of this project. I also thank my friend Ian Willard for the big help during the experimental equipment setup. This project has been sponsored by the National Science Foundation under award 1067270.